S2-08
156187

A COMPARISON OF THEORY AND EXPERIMENT FOR AEROELASTIC STABILITY OF A HINGELESS ROTOR MODEL IN HOVER

David L. Sharpe
Research Scientist
U.S. Army Aeroflightdynamics Directorate
Ames Research Center
Moffett Field, California

N88-27150

Abstract

Theoretical predictions of aeroelastic stability are compared with experimental, isolated, hingeless-rotor data. The six cases selected represent a torsionally soft rotor having either a stiff or soft pitch-control system in combination with zero precone and droop, 5° precone, or -5° droop. Analyses from Bell Helicopter Textron, Boeing Vertol, Hughes Helicopters, Sikorsky Aircraft, the National Aeronautics and Space Administration, and the U.S. Army Aeromechanics Laboratory were compared with the experimental data. The correlation ranged from very poor to fair.

Nomenclature

c	= blade chord, in.
E	= Young's modulus, lb/in.^{2}
c_ℓ, c_d, c_m	= blade section lift, drag, and pitching moment coefficients
G	= shear modulus, lb/in.^{2}
I_{EA}	= mass polar moment of inertia of the blade about the chordwise elastic axis, lb_m-in.^{2}
I_ζ	= blade-chord cross-sectional-area moment of inertia, in.^{4}
I_β	= blade-flap cross-sectional-area moment of inertia, in.^{4}
I_θ	= mass polar moment of inertia of hub components about centerline of flexure, lb_m-in.^{2}
J	= blade cross-sectional polar moment of inertia, in.^{4}
L	= blade length, start of uniform section to tip, in.
R_N	= Reynolds number of blade section
α	= blade section angle of attack, rad
β_d	= droop angle, deg
β_{pc}	= precone angle, deg
μ	= blade mass per unit length, lb_m/in.
σ	= blade lead-lag damping, sec^{-1}
θ_o	= blade pitch angle, deg
ω	= modal frequency, Hz
$\omega_{\beta NR}, \omega_{\zeta NR}, \omega_{\theta NR}$	= blade frequencies in flap, lead-lag and torsion, nonrotating model, Hz
Ω	= rotor speed, rpm

Introduction

As a part of the Methodology Assessment, six cases were selected from the experiments reported in Ref. 1. These experiments measured the lead-lag damping of a small-scale, torsionally soft hingeless rotor with uniform blade properties which was mounted on a rigid stand. The six cases included in this correlation study were chosen because they allowed a systematic study of the effects of blade precone, droop, and pitch-control stiffness on the lead-lag stability of a stiff, inplane, isolated rotor.

Eight different math models from industry and government were compared to these data. Bell Helicopter Textron used DRAV21, both with and without dynamic inflow. Boeing Vertol made the comparison with C-90. Hughes Helicopters made the comparison with the results of their time history analysis, DART. Sikorsky Aircraft used the code G400 primarily, but included some comparisons using two versions of E927. The U.S. Army Aeromechanics Laboratory made the comparisons with PFLT, and finally, NASA compared selected data points with CAMRAD.

This paper describes the experiment of Ref. 1, and compares the theoretical and experimental results. Conclusions will be made as to the quality of the correlation. Appendices are included that document the experimental model properties, tabulate the experimental data points, and show all of the correlations.

Experiment Description

A small-scale, 6.31-ft-diameter, torsionally soft, hingeless helicopter rotor was investigated in hover to determine its stability characteristics. The two-bladed, untwisted rotor was tested

on a rigid test stand at tip speeds up to 332 ft/sec. The rotor mode of interest in this investigation was the lightly damped lead-lag mode. The dimensionless lead-lag frequency of this mode was approximately 1.5/rev at 1000 rpm. The rotor was designed to allow variation in blade precone at the hub using interchangeable precone hubs, blade droop using different droop wedges, and pitch control stiffness using either a stiff or a soft pitch flexure. These features are illustrated schematically in Fig. 1. The major rotor parameters are shown in Table 1.

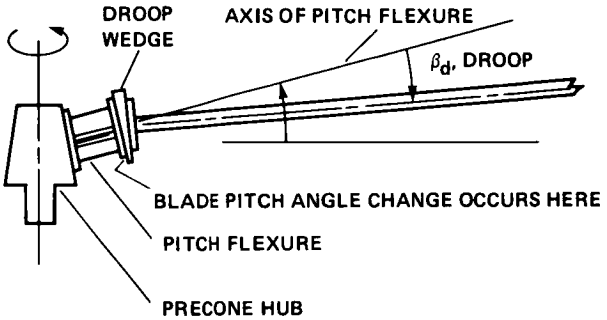

Fig. 1 Schematic of rotor hub showing precone and droop angles and location of pitch flexure.

Table 1 Experimental model properties

Variable	Value
Number of blades	2
Rotor diameter, ft	6.309
Blade length, L, ft	2.854
Blade chord, c, in.	3.4
Twist, deg	0
Nominal rotor speed, rpm	1000
R_N at tip	≈500,000
Blade frequencies at 1000 rpm, per rev	--
Flap frequency	1.15
Lead-lag frequency, stiff pitch flexure	1.50
Lead-lag frequency, soft pitch flexure	1.38
Torsional frequency, stiff pitch flexure	2.85
Torsional frequency soft pitch flexure	2.56

The model blade design is shown in Fig. 2. The blade structure was designed to minimize the blade torsional frequency while maintaining appropriate flap and lead-lag frequencies. The NACA 0012 airfoil had a unidirectional Kevlar spar, a polyurethane core, and a segmented tantalum leading edge; it was covered with fiberglass cloth. The chordwise center of gravity and the elastic axis were designed to be coincident at the blade quarter chord. The blade section stiffness and mass properties are uniform from the 9.5% radius to the tip.

An isometric view of the rotor hub components is shown in Fig. 3. The control system or pitch link flexibility is represented in the experimental model by pitch flexures mounted inboard of

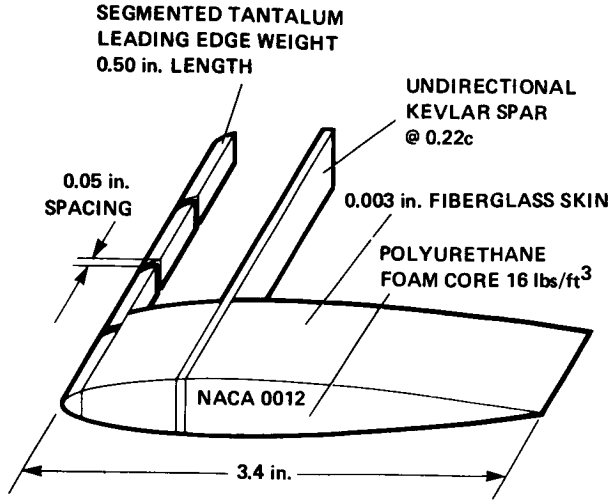

Fig. 2 Experimental-model blade design.

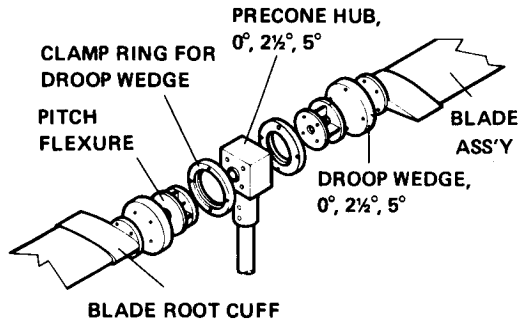

Fig. 3 Rotor hub components.

the blade. The partial cruciform cross section of these pitch flexures provides relatively high stiffness in the flap and lead-lag directions, while the torsional stiffness is controlled by the thickness of the flexure elements. Flexures of two different torsional stiffnesses were used in the experiment. Changes in precone were made with interchangeable hubs, one for each precone angle tested. Droop was varied with interchangeable droop wedges. These components were fabricated with angles of 0, ±2.5, and ±5° (positive values only for precone). In all cases the blade pitch angle was changed by rotating the blade outboard of the pitch flexure at the interface between the pitch flexure and the droop wedge. When a nonzero value of droop exists, this method of blade pitch change will introduce a small amount of blade sweep equal to the product of the blade pitch angle and the droop angle. A complete discussion of the model properties is provided in Appendix A.

The blades and associated hub components were mounted on a rigid test stand as shown in Fig. 4. Power was transmitted to the rotor shaft through a flexible belt drive. The upper truss framework which houses the drive shaft is attached to the circular mounting plate by two flexures. The lead-lag mode was excited by oscillating the upper structure about the flexures with a 50-lb electro-

ORIGINAL PAGE IS
OF POOR QUALITY

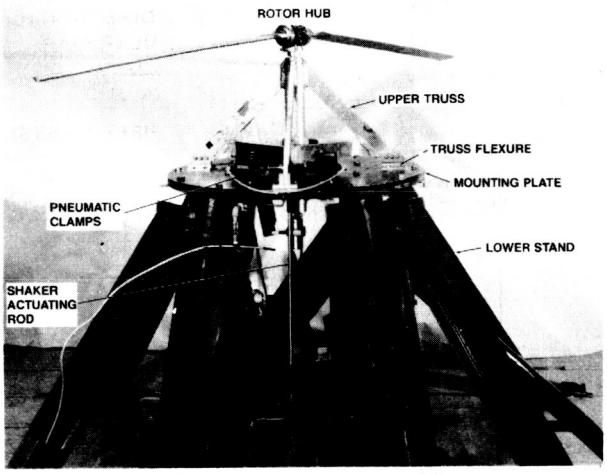

Fig. 4 Experimental rotor on test stand.

magnetic shaker. The shaker, located on the floor below the mounting plate, is attached to a forward arm of the upper truss framework by a hollow aluminum pushrod. Once sufficient lead-lag motion of the blade was obtained, the shaker excitation was shut off while a pneumatic clamp was simultaneously activated to lock the upper structure. A differential lead-lag signal was obtained by subtracting the lead-lag signal of one blade from the other to eliminate drive-system-coupling effects from the data. The lead-lag modal frequency and damping were then obtained from the differential lead-lag signal by performing a moving-block analysis on the transient decay of the blade motions.

The six experimental configurations chosen for comparison with theory in this paper are given in Table 2. The damping data shown in Fig. 5 as a

Table 2 Selected cases

Case	Pitch flexure	Precone, deg	Droop, deg
1	Stiff	0	0
2	Soft	0	0
3	Stiff	5	0
4	Soft	5	0
5	Stiff	0	-5
6	Soft	0	-5

function of pitch angle illustrate the wide variation in lead-lag damping that occurs for these cases. Figure 5a shows Cases 1 and 2, which are the least aeroelastically-coupled as there is neither precone nor negative droop. Both cases show similar behavior with pitch angle, except the damping increase is greater with the soft-pitch flexure (Case 2). The stiff-pitch-flexure cases with precone and negative droop compared in Fig. 5b show the same damping behavior. This figure shows that precone and negative droop are equivalent when the control system is stiff. Such is not the case for a soft control system as shown in Fig. 5c. The effect of control-system flexi-

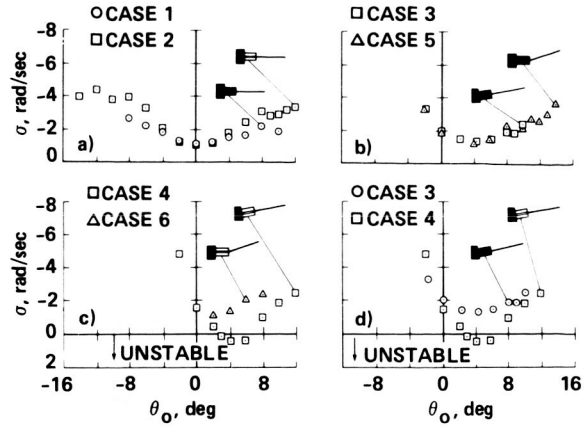

Fig. 5 Overview of experimental lead-lag damping for selected cases. a) Comparison of Cases 1 and 2 to show effects of control flexibility; b) comparison of Cases 3 and 5 to show effects of precone and droop, stiff pitch flexure; c) comparison of Cases 4 and 6 to show effects of precone and droop, soft pitch flexure; d) comparison of Cases 3 and 4 to show effects of control flexibility, 5° precone.

bility as represented here by the soft-pitch flexure is to significantly destabilize the case that includes negative droop. Figure 5d compares the cases that have 5° precone and stiff- and soft-pitch flexures. The effect of the soft-pitch flexure is to destabilize the rotor. The experimental damping data for the six cases are provided in Appendix B.

Correlation

The theoretical calculations were compared to the experimental results for the six cases by plotting lead-lag damping as a function of blade pitch. The experimental results including data scatter are shown in Figs. 6-11 as a stippled area. Table 3 provides the codes used on the figures for the various prediction methods. The appropriate predictions for each case are divided into two groups to increase clarity. The predictions shown in the upper group are those which

Table 3 Identification of prediction codes

ID	Prediction method	User
BH	DRAV21	Bell Helicopter Textron
BV	C-90	Boeing Vertol
HH_1	DART	Hughes Helicopters
SA_1	G400	Sikorsky Aircraft
SA_2	E927-2	Sikorsky Aircraft
SA_3	E927-3	Sikorsky Aircraft
AL	PFLT	U.S. Army Aeromechanics Laboratory
NA	CAMRAD	NASA Ames Research Center

were judged to be more accurate. The initial predictions using the code G400 were not considered adequate by Sikorsky Aircraft and the code was subsequently upgraded. Additional predictions were made with the upgraded code and are shown in the figures as triangular symbols without fairings. These modifications are described in detail in Ref. 2. Bell Helicopter Textron made the predictions using DRAV21 with both steady and dynamic inflow. Only the results from steady inflow are shown here. The complete comparison of theory and experiment for these six cases is included in Appendix C.

Case 1

The correlation shown in Fig. 6 is for the isolated rotor with 0° precone, 0° droop, and a stiff pitch flexure. The experimental lead-lag damping results cover both positive and negative pitch angles with minimum damping occurring at zero pitch angle. A distinct asymmetry is seen in the data, with the greater damping occurring at negative values of pitch angle.

The predictions with DRAV21 (BH) show good agreement over nearly the entire pitch-angle range tested. The point of minimum damping as well as the asymmetry in damping levels about that point are correctly predicted. The results of the Dynamic Analysis Research Tool (DART) (HH_1) were found to have fair correlation with the experiment. The DART damping prediction is shown to be symmetric for positive and negative pitch values and does not predict the reduced lead-lag damping at the higher positive blade pitch-angles that was found in the experiment. Agreement between the theory of CAMRAD (NA) and the experiment is fair, although calculations were not undertaken at the higher negative pitch-angle values. The Sikorsky analysis E927-2 (SA_2) shows fair agreement with the experimental data, with a slight underprediction of lead-lag damping over nearly the entire range of blade pitch angles. Since the damping predictions of this code are shown to be symmetric with positive and negative pitch angles, the underprediction is greater at high negative pitch-angles.

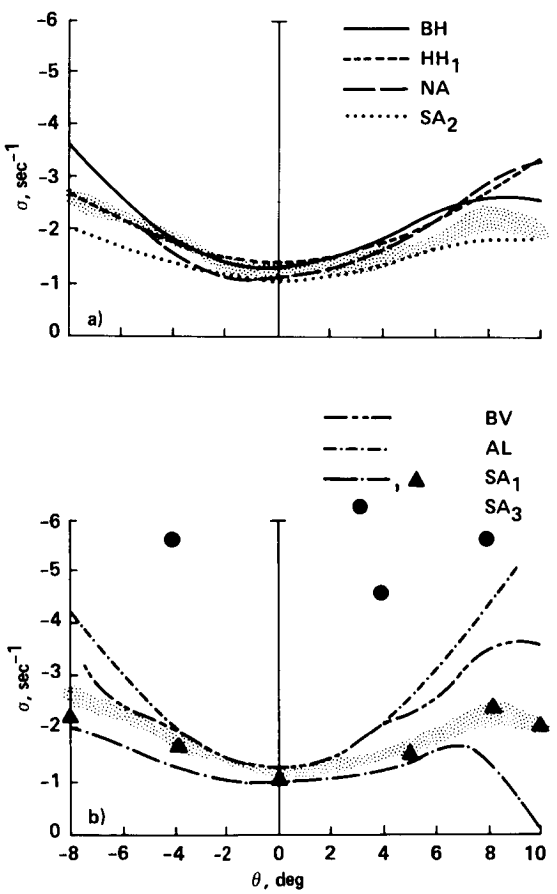

Fig. 6 Comparison of theory and experiment for Case 1; stiff pitch flexure, $\beta_{pc} = \beta_d = 0°$. a) BH, HH_1, NA, SA_2; b) BV, AL, SA_1, SA_2.

The predictions of C-90 (BV) for Case 1 are fair, showing agreement with the experimental data at negative pitch angles, but the agreement is not as good at positive pitch angles. However, the theory does show the characteristic reduction in damping at the higher positive pitch-angles. The predictions of the Aeromechanics Laboratory theory PFLT (AL) is poor-to-fair, agreeing with the test data only at low values of blade pitch angle. At pitch angles greater than 4°, agreement is poor, with the theoretically predicted increase in damping not seen in the experiment. This is probably caused by the linear representation of the aerodynamic section coefficients used in that theory. The G400 (SA_1) predictions are nearly identical to those of E927-2 (SA_2), with the exception of lead-lag damping at 10° pitch angle. The code E927-2 predicts a slight increase from the damping at 8°, whereas G400 predicts a decrease in lead-lag damping to near-neutral stability. The triangles which represent the results of the upgraded version of G400 are very good, showing a marked improvement over the original version. The theory of E927-3 (SA_3) reintroduces higher-order terms that were removed when E927-2 (SA_2) was developed from the public domain version of Ref. 3. The correlation for this code was found to be very poor. Only the lead-lag damping at zero pitch angle was predicted correctly. Damping values at blade pitch angles greater than zero were significantly overpredicted.

Case 2

The correlation shown in Fig. 7 is for a configuration having zero precone, zero droop, and a soft-pitch flexure. The increase in lead-lag damping with blade pitch angle is greater for this case than it is for Case 1. The point of minimum damping again occurs at zero pitch angle, but there is a more pronounced asymmetry about the zero point than was seen with the stiff pitch flexure.

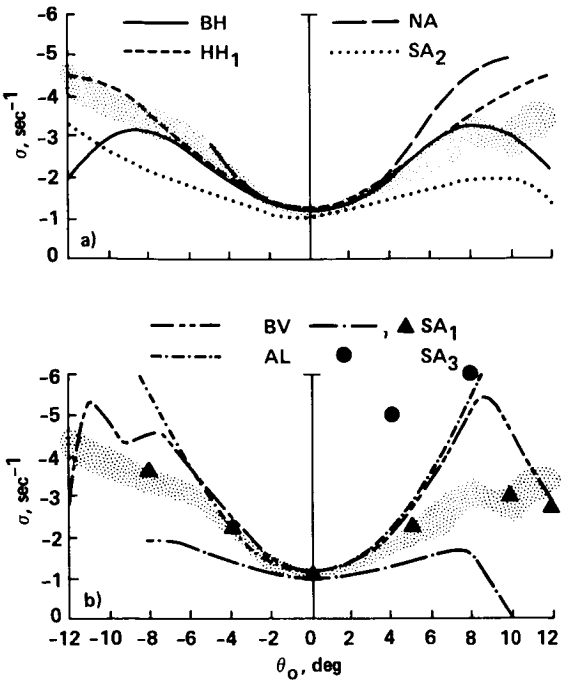

Fig. 7 Comparison of theory and experiment for Case 2; soft pitch flexure, $\beta_{pc} = \beta_d = 0°$. a) BH, HH_1, NA, SA_2; b) BV, AL, SA_1, SA_3.

The prediction of DRAV21 (BH) shows fair-to-good correlation with the experiment, but the agreement is not as good at the higher pitch angles. The theory predicts a decrease in damping due to stall above 8° which is not evident in the data. In addition, the asymmetry in damping that was correctly predicted by this theory for the stiff flexure is reversed for this case, predicting greater damping at positive blade pitch angle than at negative pitch angles. The predictions of DART (HH_1) show fair-to-good agreement with the experimental findings and show the increased lead-lag damping caused by the reduced torsional stiffness of the soft pitch flexures. The lead-lag damping predictions of CAMRAD (NA) show poor-to-fair correlation with better agreement at low pitch angles and a tendency to overpredict the damping for the higher pitch angles. The E927-2 (SA_2) code is only poor-to-fair in correlation and underpredicts the measured damping by as much as 40%. This code also shows a reduction in damping at high positive pitch angles with no change in the damping slope predicted at negative pitch angles.

The correlation of C-90 (BV) and the data are poor-to-fair, showing reasonably good agreement with the experiment at low pitch angles and an overprediction of the lead-lag damping at the higher pitch angles. This theory also predicts an asymmetry between positive and negative pitch angles, but of a different nature than was found experimentally. The weakness of the aerodynamic modeling in PFLT (AL) is again seen, with good correlation at low pitch angles and large overpredictions of lead-lag damping at high pitch angles; the overall correlation is poor-to-fair. The unmodified theory of G400 (SA_1) underpredicts the damping and again shows neutral stability at 10° pitch angle and is judged to be very poor-to-poor. The triangle symbols representing the upgraded version of G400 show greatly improved correlation. Predictions with E927-3 (SA_3) are again very poor with most lead-lag damping values being overpredicted by an order of magnitude.

Case 3

The experimental lead-lag damping results for the isolated rotor configuration having 5° of precone, 0° of droop, and the stiff pitch flexures were found to exhibit much larger changes of damping with pitch angle at low blade pitch angles than was observed for Cases 1 and 2. This is primarily due to the increased aeroelastic coupling which results from the centrifugally induced blade elastic deflection. While some of the codes were found to model this structural coupling well, others did not; this correlation is shown in Fig. 8.

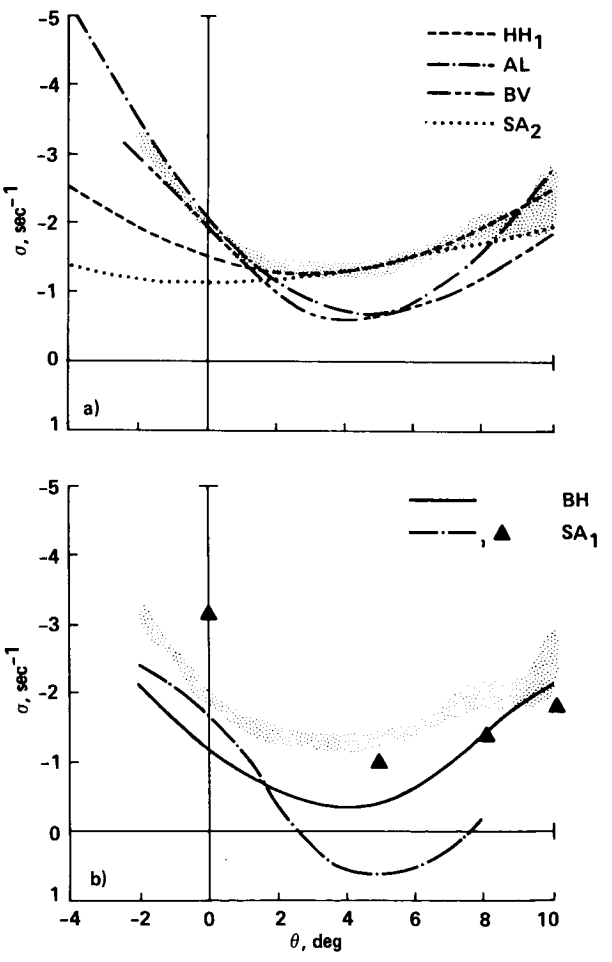

Fig. 8 Comparison of theory and experiment for Case 3; stiff pitch flexure, $\beta_{pc} = 5°$, $\beta_d = 0°$. a) HH_1, AL, BV, SA_2; b) BH, SA_1.

The lead-lag damping predictions of DART (HH_1) are good at the positive values of pitch angle where the equilibrium deflections and coupling which results are low. However, the quality of the correlation deteriorates as this equilibrium deflection and coupling grows with increasing negative pitch angle, and the overall agreement is considered fair. The theory of PFLT (AL) shows good correlation with the experiment over the negative pitch-angle range where the coupling is large, but underpredicts the damping at positive pitch angles, so overall is judged to be fair. The C-90 analysis (BV) exhibits nearly the same predictive characteristics as PFLT and also is considered to be fair. The E927-2 code (SA_2) shows agreement with the experiment at high positive pitch angles, but where the coupling is strong and the damping should show a marked increase, the predictions show little change. A comparison of Cases 1 and 3 shows that the E927-2 predictions are identical, and neither precone nor droop affect the predicted value. The correlation is judged to be poor. The DRAV21 code (BH) successfully predicts the experimental trend in lead-lag damping with pitch angle, but consistently underpredicts the experimental results, so is only considered to be poor-to-fair. The G400 analysis (SA_1) shows very poor correlation with the experimental results in the original version, predicting an instability between 2.5 and 7.5° pitch angle. The modified version of G400, shown by the triangle symbols, shows fair correlation with the experiment, with no predicted instability. The E927-3 version (SA_3) was unable to predict lead-lag stability characteristics for this case.

Case 4

The experimental lead-lag damping results for the configuration with 5° of precone and 0° of droop with soft-pitch flexures show the rotor to be dynamically unstable between 2.5 and 7° pitch angle. Nearly all the math models predict this instability but with varying degrees of accuracy. The correlation is shown in Fig. 9.

The theoretical predictions from PFLT (AL) show fair-to-good correlation with the experimental results. The pitch angle range at which the instability occurs is well predicted. The severity of the instability is slightly overpredicted and the damping at high pitch angles is also overpredicted. The correlation with DART (HH_1) shows fair agreement, with the degree of instability being somewhat underpredicted when compared to the experiment. The DRAV21 (BH) and C-90 (BV) results are nearly identical, both showing poor-to-fair correlation. The damping trend with pitch angle follows the experiment closely; however, the pitch angle range and degree of instability are substantially overpredicted. The original version of G400 (SA_1) also severely overpredicts the magnitude and range of the instability, showing nearly the same correlation as DRAV21 and C-90. The modified version of G400, shown by the triangle symbols, gives somewhat mixed

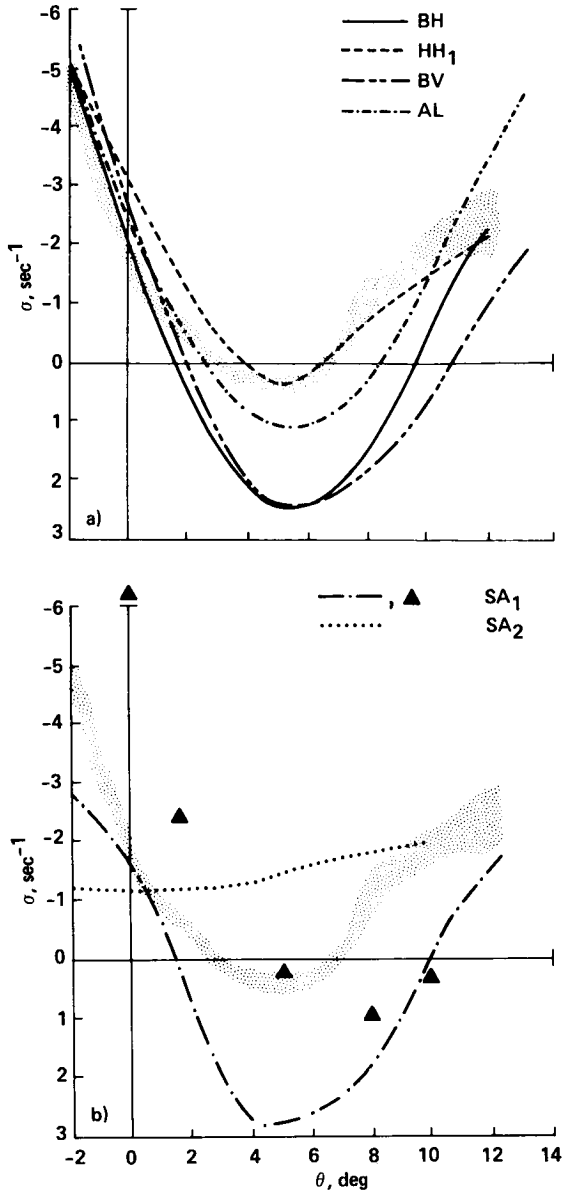

Fig. 9 Comparison of theory and experiment for Case 4; soft pitch flexure, β_{pc} = 5°, β_d = 0°. a) BH, HH_1, BV, AL; b) SA_1, SA_2.

results. Although the extent of the instability is reduced and is in better agreement with the experiment, the pitch-angle range where the instability occurs shows poorer correlation than with the unmodified version of G400. The E927-2 code shows very poor correlation and fails to predict the instability.

Case 5

The correlation shown in Fig. 10 is for the configuration with 0° precone, -5° droop, and stiff-pitch flexures. When the experimental results for this case are compared with Case 3 (Fig. 5b), the damping results are seen to be

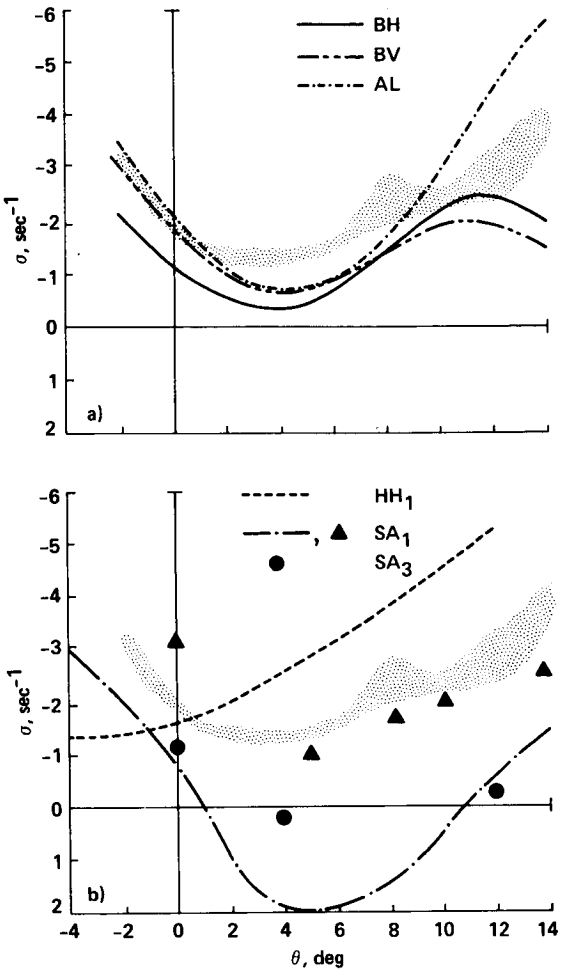

Fig. 10 Comparison of theory and experiment for Case 5; stiff pitch flexure, β_{pc} = 0°, β_d = -5°. a) BH, BV, AL; b) HH_1, SA_1, SA_3.

nearly identical. In general, the predictions of the analytical codes also show this correspondence.

The DRAV21 (BH), C-90 (BV), and PFLT (AL) codes each confirm that without control system flexibility, the 5° precone and -5° droop are dynamically the same. The correlation of these three codes is essentially the same as observed in Case 3.

The damping predictions of DART (HH_1) did not agree with the experimental results for this configuration, nor did it show any similarity to the DART prediction for Case 3 because the sign convention in the input of the droop angle was reversed. The original version version of G400 (SA_1) shows very poor correlation, with the theory predicting an instability where none existed. With modifications, the instability was no longer predicted and the overall correlation improved. Predictions with E927-3 (SA_3) were again very poor.

Case 6

The correlation for a configuration having 0° precone, -5° of droop, and soft pitch flexures is shown in Fig. 11. Although the experimental data show that the damping characteristics for this case are roughly the same as Case 5, the theoretical models show different results.

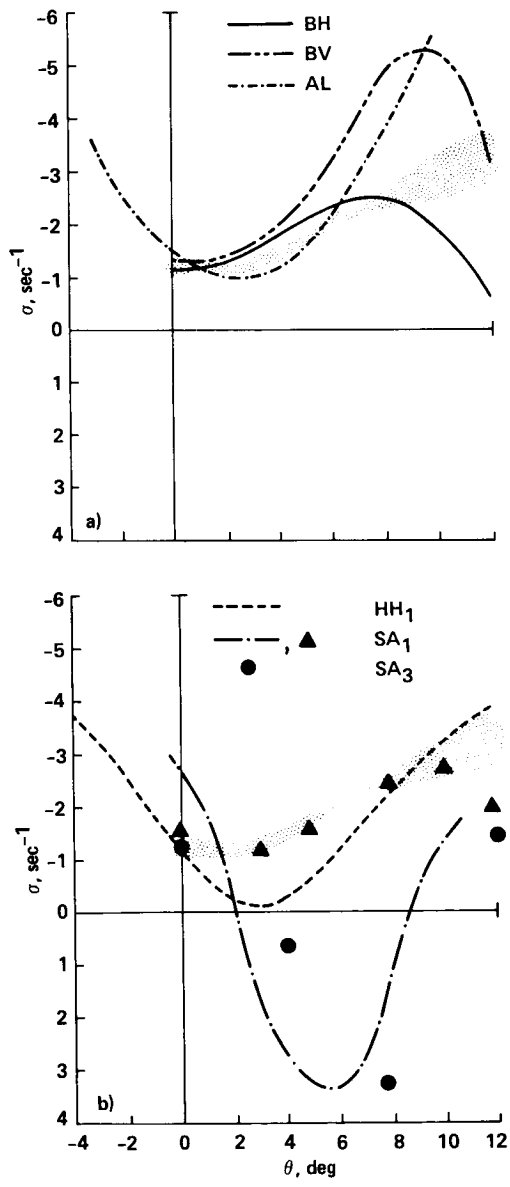

Fig. 11 Comparison of theory and experiment for Case 6; soft pitch flexure, β_{pc} = 0°, β_d = -5°. a) BH, BV, AL; b) HH_1, SA_1, SA_3.

The DRAV21 (BH), C-90 (BV), and PFLT (AL) codes show fair correlation with the experimental data at low blade-pitch angles, but the correlation becomes progressively worse as the pitch angle increases. The predicted damping for the

three codes is vastly different beyond 5°. The computer code DRAV21 (BH) agrees reasonably well with the experimental results up to about 8° blade pitch angle, at which point an abrupt decrease in damping with increasing blade pitch is predicted, with the theory substantially underpredicting the experimental results. Overall the correlation is considered to be fair. The computer code C-90 (BV) shows reasonable agreement with the experimental data for only the first 3 or 4° of blade pitch angle. At higher blade pitch angles, the correlation degrades, with the theory predicting nearly twice as much damping at about 8° pitch and a sharp reduction of damping with pitch angle beyond 10°. The correlation over the pitch-angle range is judged poor. The code PFLT (AL) shows fair agreement up to approximately 6° blade pitch angle, but increasingly overpredicts the damping beyond this value, and the overall correlation is poor-to-fair.

The correlation between the experiment and the theory for DART (HH) is poor, with the theory substantially underpredicting the experimental damping over most of the pitch-angle range and with the predictions approaching neutral stability at between 3 and 4°.

Predictions with the unmodified G400 (SA_1) were found to be very poor, showing a strong instability over much of the pitch-angle range. On the other hand, the modified version of the G400 shows very good correlation with the experimental results, with the exception of the highest pitch-angle setting where the damping is underpredicted. The E927-3 (SA_3) predictions again show very poor correlation with the experimental data.

Conclusions

Eight analyses were compared with one or more cases selected from an experiment that measured the damping of an isolated, torsionally soft rotor in hover.

1. The DRAV21 analysis used by Bell Helicopter Textron was considered to give fair correlation overall for the six cases.

2. The C-90 analysis used by Boeing Vertol was judged to have poor-to-fair correlation overall.

3. The DART analysis used by Hughes Helicopters was also considered to have poor-to-fair capability when compared to the six cases.

4. Sikorsky Aircraft used the analysis code G400 and two versions of E927: E927-2 and E927-3. Overall the G400 code was judged as very poor-to-poor, and the E927-2 and E927-3 analyses were considered poor and very poor, respectively. Subsequent to the evaluation the G400 code was upgraded and limited results are shown for the six cases. These results show that the G400 code has been substantially improved.

5. The Aeromechanics Laboratory PFLT analysis was considered to provide fair correlation.

6. The NASA Ames CAMRAD calculations were made for two cases and were judged to be fair.

References

[1]Sharpe, David L., "An Experimental Investigation of the Flap-Lag-Torsion Aeroelastic Stability of a Small Scale Hingeless Helicopter Rotor in Hover," NASA TP-2546, Jan. 1986.

[2]Bielawa, Richard L., "Considerations of Spanwise Variable Elastic Axis Offset in the Aeroelastic Modelling of Rotor Blades," NASA CP 10007, May 1988.

[3]Johnston, R. A. and Cassarino, S. J., "Aeroelastic Rotor Stability Analysis," USAAMRDL TR 75-40, Jan. 1976.

[4]Hodges, D. H. and Ormiston, R. A., "Stability of Elastic Bending and Torsion of Uniform Cantilever Rotor Blades in Hover with Variable Structural Coupling," NASA TN D-8192, April 1976.

[5]Hodges, D. H., "Nonlinear Equations of Motion for Cantilever Rotor Blades in Hover with Pitch Link Flexibility, Twist, Precone, Droop, Sweep, Torque Offset, and Blade Root Droop," NASA TM X-73,122, May 1976.

[6]Hodges, Dewey H. and Ormiston, R. A., "Stability of Hingeless Rotor Blades in Hover with Pitch-Link Flexibility," AIAA Journal, Vol. 15, No. 4, April 1977, pp. 476-482.

[7]Ormiston, R. A. and Bousman, W. G., "A Study of Stall-Induced Flap-Lag Instability of Hingeless Rotors," Preprint No. 730, American Helicopter Society 29th Annual National Forum, May 1973.

Appendix A--Model Properties

The six cases of experimental data presented in this paper are from an investigation originally reported in Ref. 1. The model properties included in this appendix have been taken from that reference. The rotor blades and associated hub hardware were specifically designed and built to match as closely as possible the theory presented in Refs. 4-6. The experimental model was built with uniform blade properties and simple hub hardware. Prior to the stability investigation, an extensive bench test program was undertaken to measure the mass and stiffness properties. In many cases more than one method was used for these measurements to assure the most accurate estimate. Where measurements were not possible, calculated values are used. A number of experimental model properties have been given in Table 1 of the main text. Additional model properties are presented in this appendix.

Rotor Mass and Stiffness Properties

The spanwise distributions of weight, stiffness, and mass polar moment of inertia of the rotor configuration having the soft pitch flexure are shown in Table 4. The radial location of the hub hardware components is shown in Fig. 12. The spanwise dimension of the soft flexure web is greater than that of the stiff flexure web to minimize its torsional stiffness. The tabulated properties in Table 4 from blade station (B.S.) 0.701 to 3.601 in. were calculated from design drawings except for the torsional stiffness of the pitch flexure (B.S. 0.726 to 1.626 in.). The pitch flexure torsional stiffness was estimated using two methods: the moment-deflection method and the frequency-inertia method. In the moment-deflection method, known moments were applied outboard of the flexure and its angular deflection was measured. In the frequency-inertia method, the frequency of the torsional spring-mass system was measured after attaching a steel bar or disk with a known polar moment of inertia to the outer flange. The torsional stiffness estimated by the moment-deflection method was 12% lower than that obtained using the frequency-inertia method. The latter method is considered more accurate so this value is used in Table 4.

The properties of the stiff-pitch-flexure rotor are the same as the soft pitch flexure except from B.S. 0.726 to 1.626 in. Over this span the properties can be determined from the pitch flexure geometry as given in Table 5.

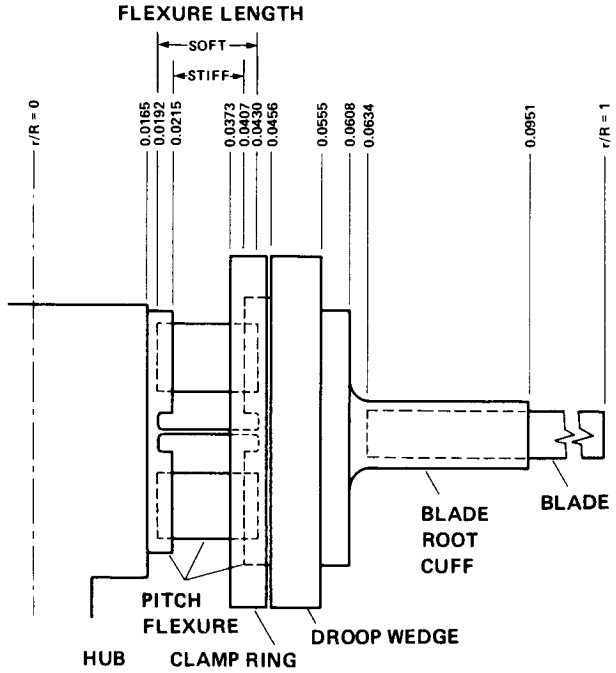

Fig. 12 Radial location of model rotor hub and blade components.

The blade mass properties outboard of B.S. 3.601 in., which is the start of the uniform section, have been determined from measurements

Table 4 Rotor mass and stiffness properties distribution for blade with soft pitch flexure

Blade station, in.	Weight, lb/in.	EI_β, lb-in.^{2} (10^6)	EI_ζ, lb-in.^{2} (10^6)	GJ, lb-in.^{2} (10^6)	I_θ, lb-in.^{2}/in.
0.701	0.292	20.0	20.0	19.6	
0.726	0.292	0.161	0.199	0.000327	
0.813	0.292	0.161	0.199	0.000327	
0.813	0.0115	0.161	0.199	0.000327	
1.415	0.0115	0.161	0.199	0.000327	
1.415	0.303	0.161	0.199	0.000327	
1.539	0.303	0.161	0.199	0.000327	0.543
1.539	0.560	0.161	0.199	0.000327	0.543
1.626	0.560	0.161	0.199	0.000327	0.543
1.651	0.560	21.9	21.9	19.6	0.543
1.665	0.560	21.9	21.9	19.6	0.543
1.665	0.713	21.9	21.9	19.6	0.543
1.726	0.713	21.9	21.9	19.6	0.543
1.726	0.558	27.2	27.2	19.8	0.494
2.101	0.558	27.2	27.2	19.8	0.494
2.101	0.295	18.2	18.2	7.28	0.165
2.301	0.295	18.2	18.2	7.28	0.165
2.301	0.149	0.300	30.3	1.80	0.213
2.401	0.149	0.300	30.3	1.80	0.213
2.401	0.136	0.242	21.8	1.66	0.213
3.601	0.136	0.242	21.8	1.66	0.213
3.601	0.0193	0.00589	0.120	0.00177	0.0179
37.851	0.0193	0.00589	0.120	0.00177	0.0179

Table 5 Pitch flexure dimensions

Flexure	A, in.	B, in.	Inboard blade station, in.	Outboard blade station, in.
Stiff	0.200	0.200	0.813	1.539
Soft	0.018	0.023	0.726	1.626

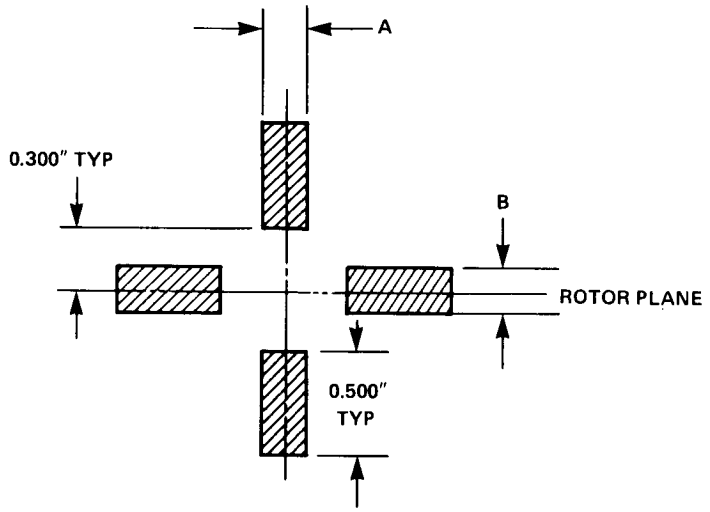

made on a 35.45-in. length of blade that included a 1.20-in. fiberglass cuff core. These properties were then corrected from measurements made on a separate cuff core and are given in Table 6. The values in Table 6 represent the average of two blades. The mass was determined by weighing the blades on an electronic balance. The uniform blade total-mass polar moment of inertia was measured by swinging the blades as a pendulum about the trailing edge. The blade was suspended from tape at two locations and allowed to swing freely as a pendulum. The pendular frequency was measured by an electronic counter connected to a photo cell that counted the number of interruptions of a light beam by the oscillating blade. The blade mass moment of inertia about the trailing edge was transferred to the elastic axis and is shown in Table 6.

Additional properties measured on the uniform section and given in Table 6 were the blade center of gravity and location of the elastic axis. The center of gravity was measured by using a fixture that allowed the blade to be supported between a fixed point and an electronic balance. The chord elastic axis was experimentally determined by mounting each blade vertically in a rigid fixture and applying a normal load in flapping through a slide-mounted pointer. The torsional deflection was monitored with an optical system using a mirror bonded to the blade tip and a light collimator.

Table 6 Uniform blade section properties

Property	Value
Weight, lb	0.659
Mass polar moment of inertia, lb_m-in.^{2}	0.613
Center of gravity, percent c	24.8
Elastic axis, percent c	25.3

The blade flapwise, chordwise, and torsional stiffness outboard of B.S. 3.601 in. were determined by two separate methods. The first method used force-deflection measurements for the flap and lead-lag stiffness and used moment-deflection measurements for the torsional stiffness; however, there was difficulty in measuring slight rotations of the mounting fixture. The second method used the measured frequencies and blade mass properties to calculate the stiffnesses. Frequencies were easily measured within ±1%, and blade weight was also determined within this accuracy. The stiffness was then derived from elementary beam theory as

$$EI_\beta = \frac{1}{12.4}\,\mu L^4(\omega_{\beta NR})^2$$

$$EI_\zeta = \frac{1}{12.4}\,\mu L^4(\omega_{\zeta NR})^2$$

$$GJ = 4LI_{EA}\,\frac{(\omega_{\theta NR})^2}{\pi}$$

The flapping and torsional stiffness values obtained by the two methods were within 4 and 2%, respectively. However, the value for lead-lag stiffness obtained by the force-deflection method was approximately 12% below the frequency-mass measurement. Because of the difficulty in accurately measuring fixture rotation, the frequency-mass and frequency-inertia measurements were used for the blade stiffnesses in Table 4.

The weight and mass polar of inertia for the hub components shown in Table 7 were each determined experimentally. The weights were determined by weighing each component on an electronic balance. The mass moment of inertia of each component was experimentally determined using a

Table 7 Hub component mass and inertia properties

Hub component	Weight, lb	Polar moment of inertia, I_θ, lb_m-in.^{2}
Flexure flange	0.100[a]	0.05487[a]
Clamp ring	0.065	0.1151
Droop wedge	0.207	0.206
Root cuff	0.165	0.256
Cuff core	0.071	0.061
TOTAL	0.608	0.693

[a]Calculated.

with a known spring constant. The component was mounted to the strain-gaged torsional spring. Then the frequency of the torsional spring/mass combination was measured and the mass polar moment of inertia was determined.

Nonrotating tests were conducted to determine modal frequencies and lead-lag structural damping. With the rotor stand clamped, each mode was manually excited and resulting oscillations were analyzed. The results for the first four modes for cases 1 and 2 are shown in Table 8.

Table 8 Rotor frequency and damping

	Stiff flexure		Soft flexure	
	ω, Hz	σ, sec^{-1}	ω, Hz	σ, sec^{-1}
First flap mode	5.25	--	5.19	--
Second flap mode	32.75	--	32.50	--
First lead-lag mode	23.76	-1.23	22.02	-1.03
First torsion mode	44.73	--	38.38	--

Aerodynamic Section properties

The blade profile used for the model was an NACA 0012. The Reynolds number at 0.75 R is approximately 375,000. The section aerodynamic properties are represented by the analytic functions that were used in Ref. 7.

$$C_\ell = 6\alpha - (\text{sgn}\ \alpha)10\alpha^2$$

$$C_d = 0.01 + 11.1|\alpha|^3$$

$$C_m = 0$$

Appendix B--Experimental Data

The experimental data for Cases 1 through 6 are tabulated in Tables 9 through 14, respectively. These data were obtained in the experiment reported in Ref. 1. The lead-lag damping and blade pitch angle are shown at 1000 rpm for all the cases. The data for the differential lead-lag mode were obtained by exciting the rotor hub with an electromagnetic shaker and the damping was obtained from the transient decay of the motions after the excitation was stopped. A moving block analysis of that transient decay was used to estimate the modal damping.

Appendix C--Correlation

The complete set of correlations between all theoretical predictions and the selected experimental results is shown in Figs. 13-34. Two formats are used for the correlation. The first format compares each individual code with the experimental data on separate plots. In this format the actual calculated points are shown as solid symbols and the fairing between points was made by the analyst. The experimental data are shown as open symbols. The second format compares all the predictions with the experimental results on a composite plot with the data shown as a stippled area. The theory of DRAV21 (BH) is shown with and without dynamic inflow. A legend for the codes that were used is given in Table 3.

Table 9 Case 1 blade pitch angle and lead-lag damping; stiff pitch flexure, $\beta_{pc} = \beta_d = 0°$

θ_o, deg	σ, sec^{-1}	θ_o, deg	σ, sec^{-1}
-8.0	-2.81	4.0	-1.56
-8.0	-2.55	6.0	-1.87
-6.0	-2.25	6.0	-1.68
-6.0	-2.36	8.0	-2.14
-4.0	-1.88	8.0	-2.45
-2.0	-1.34	8.0	-2.11
-2.0	-1.38	10.0	-2.02
0.0	-1.19	10.0	-1.96
4.0	-1.53		

Table 10 Case 2 blade pitch angle and lead-lag damping; soft pitch flexure, $\beta_{pc} = \beta_d = 0°$

θ_o, deg	σ, sec^{-1}	θ_o, deg	σ, sec^{-1}
-12.0	-4.31	4.0	-1.86
-12.0	-4.72	4.0	-1.89
-12.0	-4.17	6.0	-2.05
-12.0	-4.44	6.0	-2.84
-12.0	-4.03	6.0	-2.51
-10.0	-3.99	8.0	-2.92
-10.0	-3.70	8.0	-3.01
-10.0	-3.71	8.0	-3.40
-10.0	-3.57	9.0	-2.68
-10.0	-3.66	9.0	-2.89
-8.0	-4.07	9.0	-2.97
-8.0	-3.74	9.0	-2.86
-8.0	-4.21	10.0	-2.75
-6.0	-3.21	10.0	-3.45
-6.0	-3.25	10.0	-2.52
-4.0	-2.10	10.0	-2.79
-4.0	-2.22	10.0	-3.17
-2.0	-1.29	11.0	-3.19
-2.0	-1.38	11.0	-3.01
0.0	-1.05	11.0	-3.76
2.0	-1.27	12.0	-3.31
2.0	-1.20	12.0	-3.32

Table 11 Case 3 blade pitch angle and lead-lag damping; stiff pitch flexure, $\beta_{pc} = 5°$, $\beta_d = 0°$

θ_o, deg	σ, sec^{-1}	θ_o, deg	σ, sec^{-1}
-2.0	-3.31	6.0	-1.53
-2.0	-3.25	8.0	-1.88
0.0	-1.92	8.0	-2.14
0.0	-1.96	8.0	-1.97
2.0	-1.44	9.0	-1.86
2.0	-1.43	9.0	-2.07
4.0	-1.35	9.0	-2.00
4.0	-1.29	10.0	-2.16
6.0	-1.48	10.0	-2.87

Table 12 Case 4 blade pitch-angle and lead-lag damping; soft pitch flexure, $\beta_{pc} = 5°$, $\beta_d = 0°$

θ_o, deg	σ, sec^{-1}	θ_o, deg	σ, sec^{-1}
-2.0	-4.92	8.0	-0.93
-2.0	-4.84	8.0	-1.44
0.0	-1.67	8.0	-0.94
0.0	-1.57	8.0	-0.97
0.0	-1.55	10.0	-1.80
2.0	-0.45	10.0	-2.16
2.0	-0.44	10.0	-1.74
2.0	-0.54	12.0	-2.76
3.0	0.10	12.0	-2.79
4.0	0.24[a]	12.0	-1.90
6.0	0.30[b]		

[a]Extrapolated; nearest test value: Ω = 993 rpm, σ = +0.13 sec^{-1}.
[b]Extrapolated; nearest test value: Ω = 997 rpm, σ = +0.23 sec^{-1}.

Table 13 Case 5 blade pitch angle and lead-lag damping; stiff pitch flexure, $\beta_{pc} = 0°$, $\beta_d = -5°$

θ_o, deg	σ, sec^{-1}	θ_o, deg	σ, sec^{-1}
-2.0	-3.29	8.0	2.30
0.0	-1.95	10.0	2.79
0.0	-1.79	10.0	2.84
0.0	-1.92	11.0	2.37
2.0	1.45	11.0	2.38
2.0	1.38	12.0	3.21
4.0	1.38	12.0	2.93
4.0	1.50	12.0	2.94
4.0	1.50	13.0	-3.47
6.0	2.71	13.0	-2.73
6.0	1.99	14.0	-4.07
8.0	2.08	14.0	-3.61
8.0	2.24	14.0	-3.48

Table 14 Case 6 blade pitch angle and lead-lag damping; soft pitch flexure, $\beta_{pc} = 0°$, $\beta_d = -5°$

θ_o, deg	σ, sec^{-1}	θ_o, deg	σ, sec^{-1}
0.0	-1.22	6.0	-2.07
0.0	-1.21	8.0	-2.37
0.0	-1.30	8.0	-2.43
2.2	-1.22	10.0	-2.51
2.2	-1.20	10.0	-3.09
2.2	-1.09	10.0	-2.52
4.0	-1.41	10.0	-2.57
4.0	-1.38	12.0	-3.45
4.0	-1.38	12.0	-3.11
6.0	-2.05	12.0	-2.82
6.0	-2.06		

ORIGINAL PAGE IS
OF POOR QUALITY

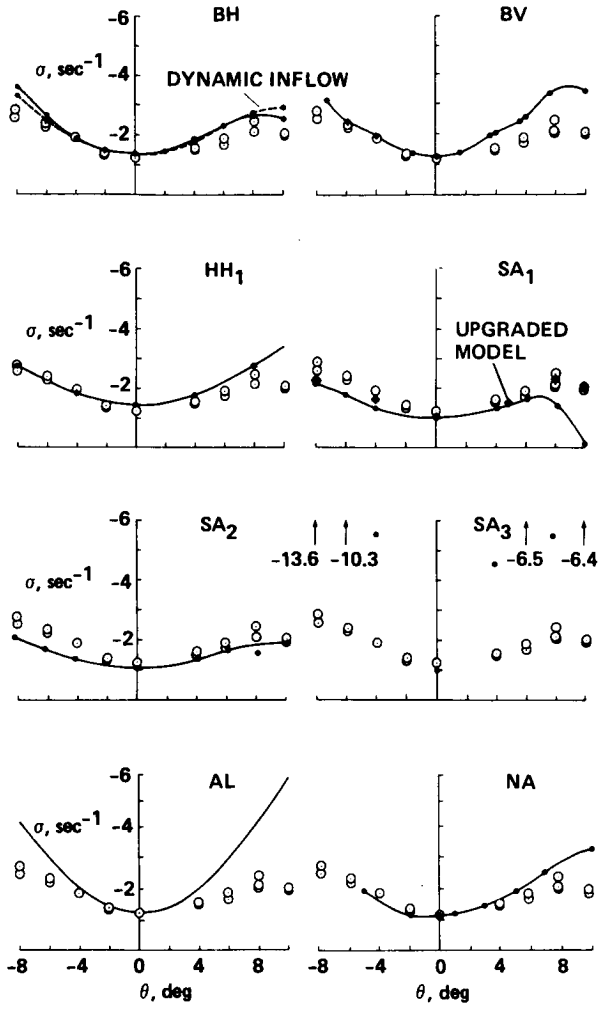

Fig. 13 Individual comparison for Case 1 lead-lag damping; stiff pitch flexure, $\beta_{pc} = \beta_d = 0°$.

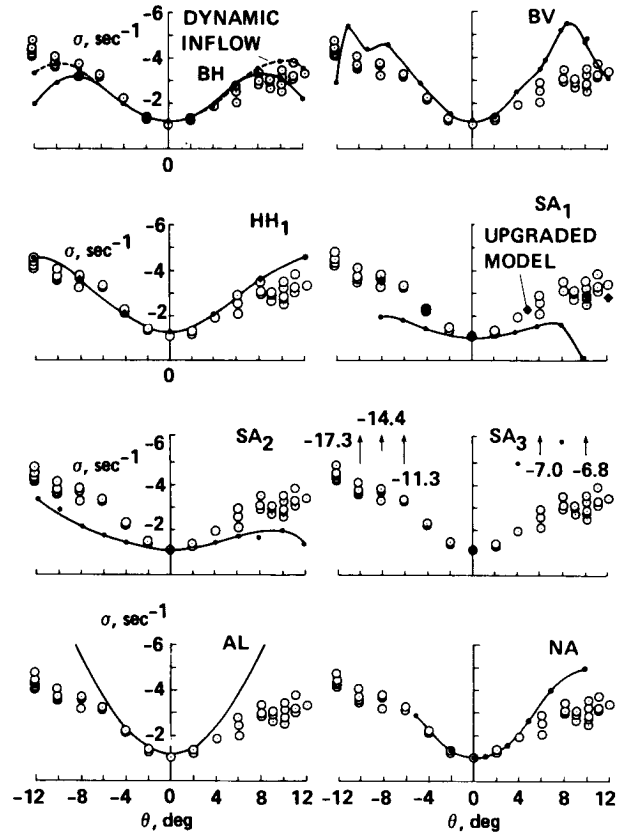

Fig. 15 Individual comparison for Case 2 lead-lag damping; stiff pitch flexure, $\beta_{pc} = \beta_d = 0°$.

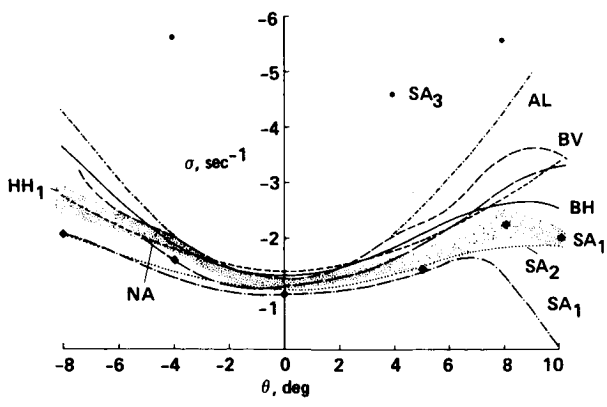

Fig. 14 Composite comparison for Case 1 lead-lag damping; stiff pitch flexure, $\beta_{pc} = \beta_d = 0°$.

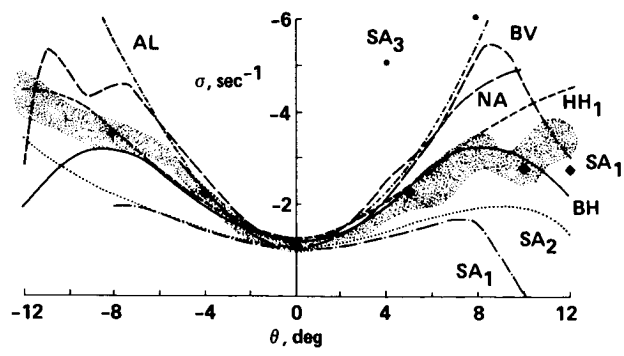

Fig. 16 Composite comparison for Case 2 lead-lag damping; soft-pitch flexure, $\beta_{pc} = \beta_d = 0°$.

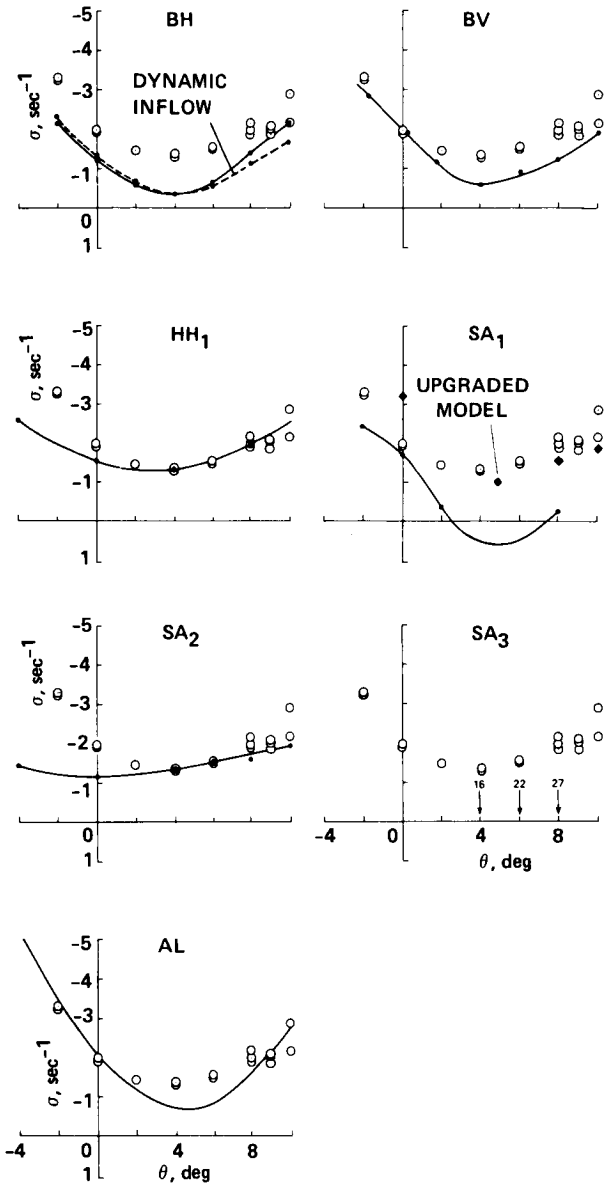

Fig. 17 Individual comparison for Case 3 lead-lag damping; stiff pitch flexure, β_{pc} = 5°, β_d = 0°.

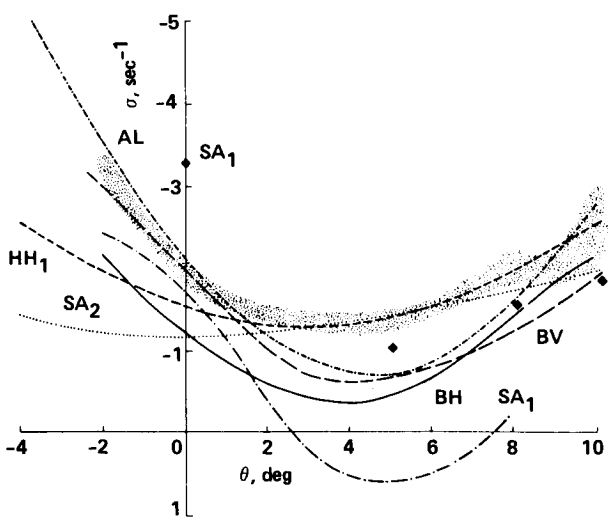

Fig. 18 Composite comparison for Case 3 lead-lag damping; stiff pitch flexure, β_{pc} = 5°, β_d = 0°.

ORIGINAL PAGE IS
OF POOR QUALITY

ORIGINAL PAGE IS
OF POOR QUALITY

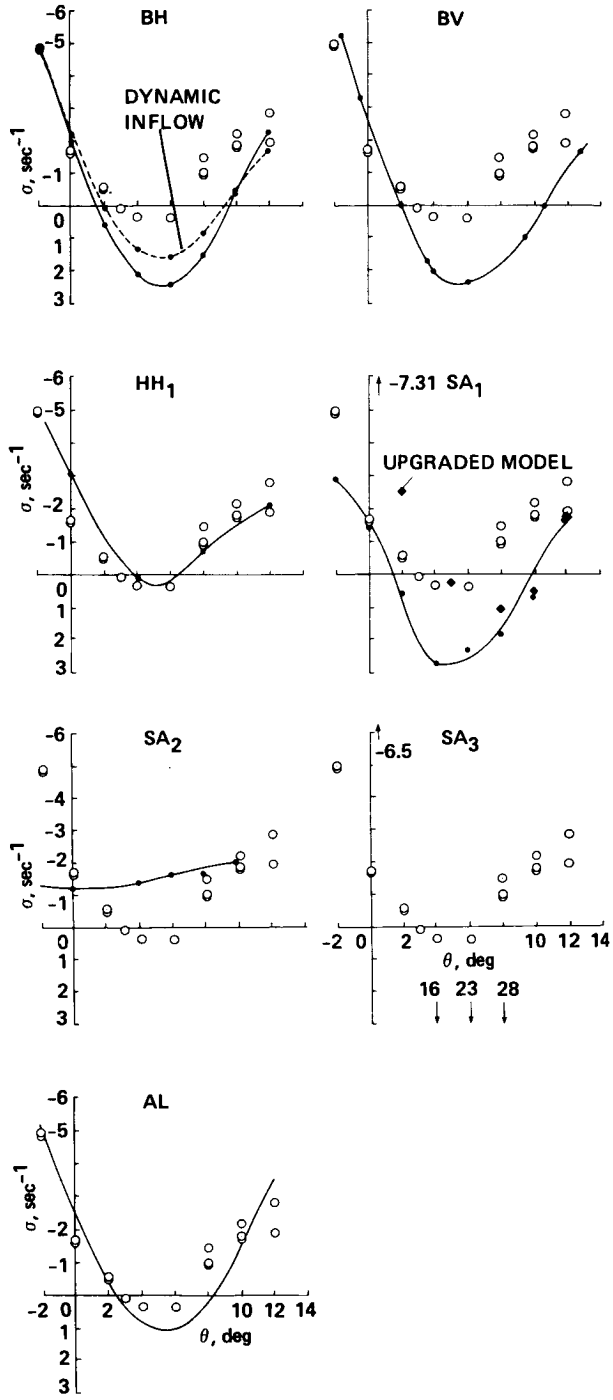

Fig. 19 Individual comparison for Case 4 lead-lag damping; soft pitch flexure, β_{pc} = 5°, β_d = 0°.

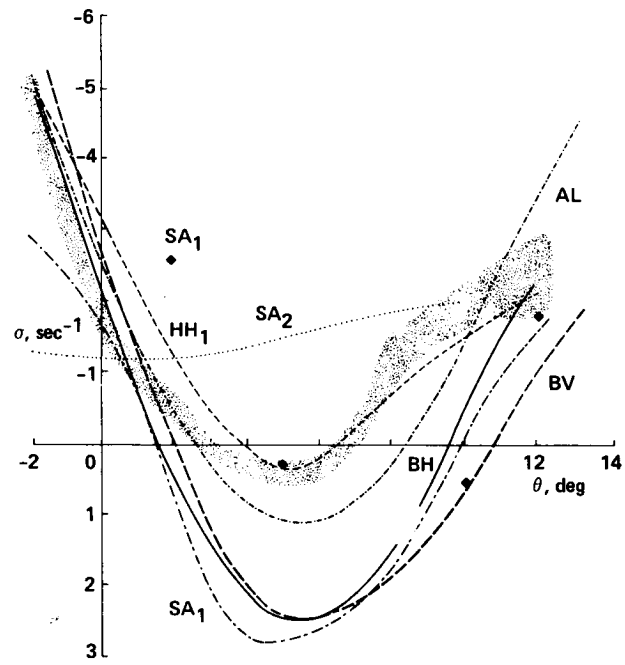

Fig. 20 Composite comparison for Case 4 lead-lag damping; soft pitch flexure, β_{pc} = 5°, β_d = 0°.

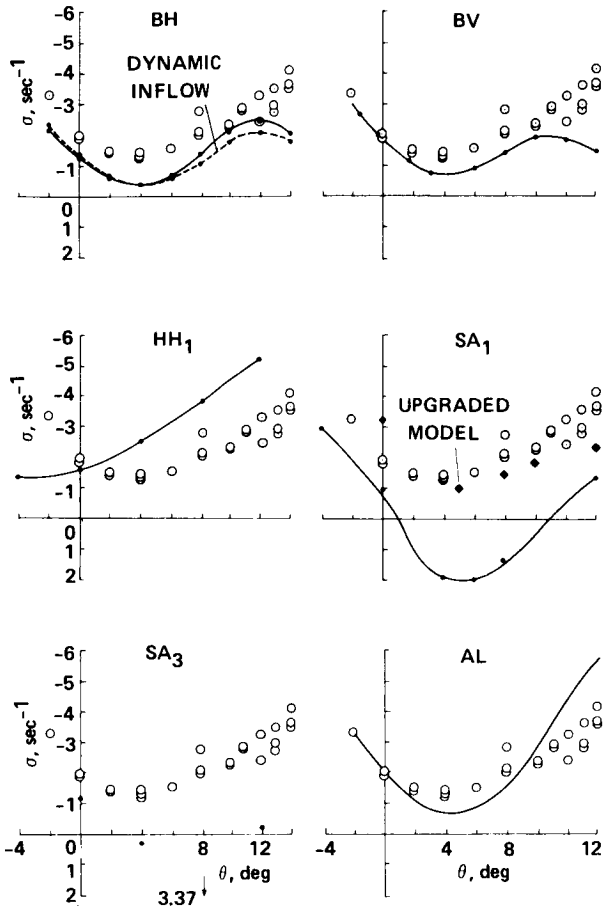

Fig. 21 Individual comparison for Case 5 lead-lag damping; stiff pitch flexure, β_{pc} = 0°, β_d = -5°.

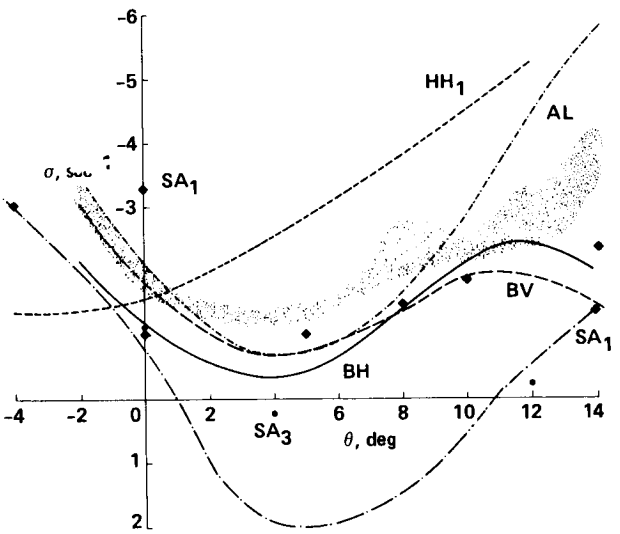

Fig. 22 Composite comparison for Case 5 lead-lag damping; stiff pitch flexure, β_{pc} = 0°, β_d = -5°.

ORIGINAL PAGE IS
OF POOR QUALITY

ORIGINAL PAGE IS
OF POOR QUALITY

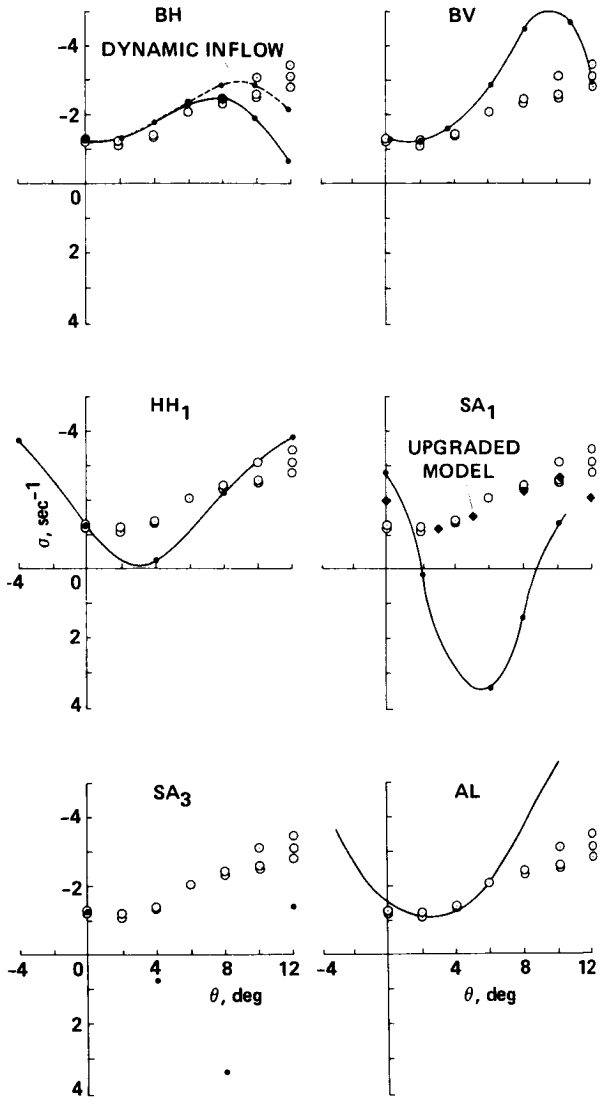

Fig. 23 Individual comparison for Case 6 lead-lag damping; soft pitch flexure, β_{pc} = 0°, β_d = -5°.

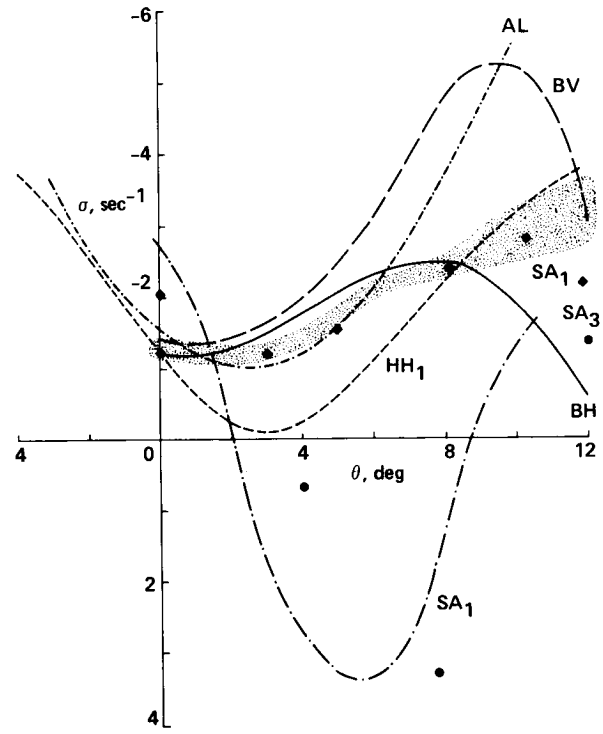

Fig. 24 Composite comparison for Case 6 lead-lag damping; soft pitch flexure, β_{pc} = 0°, β_d = -5°.